Development of a High Power Density Drive System for Unmanned Aerial Vehicles

Martin Schiestl, Federico Marcolini, *Student Member, IEEE*, Maurizio Incurvati, *Member, IEEE*,
Fabio Giulii Capponi, *Member, IEEE*, Ronald Stärz, Federico Caricchi, *Member, IEEE*,
Alejandro Secades Rodríguez, and Lukas Wild

***Abstract*—Unmanned aerial vehicles are characterized by a set of requirements, like high efficiency, resiliency, and reliability that conflict with the other main requirement of high power density aimed at minimizing the overall weight and size. This article proposes a novel, modular multiphase drive for a quadrotor drone, realized through the integration of an axial flux permanent magnet machine and a GaN-based power electronic converter. After an overview of the design process, starting from the propeller choice, a brief description of the system components is presented. Focusing specifically on the power electronic converter, the article then presents a full analysis of its electrical and thermal performance. Extensive experimental tests allows to validate the predictions of the design and simulation stages and demonstrated the expected high power density levels.**

***Index Terms*—Aerospace safety, fault tolerance, gallium nitride, integrated design, motor drives, thermal analysis, thermal modeling, unmanned aerial vehicles (UAVs), variable speed drives.**

I. INTRODUCTION

DRONES are unmanned aerial vehicles (UAVs) that can fly, autonomously or remotely piloted, in open or in confined spaces, for thousand kilometers or just for few minutes. UAVs are therefore designed with very different structures and sizes, according to the expected performances. One of the most common structure is the so-called multirotor UAV, commonly named also vertical take-off and landing [1], [2]. It has hoovering capabilities and can fly in every direction, horizontally and vertically, with high maneuverability [3]. Because of their versatility, multirotor UAVs are gaining more and more interest in a variety of commercial and military applications such as: delivery, ambulance, bushfire monitoring, agriculture, or surveillance drones [4]–[7].

Regardless of the mission type, the main challenges in multirotor UAVs design are dictated by the need to maximize payload, maneuverability, and flight endurance. Payload and maneuverability are related to the size and weight of its propulsion components and therefore to their power density. On the other side, the flight endurance depends on the stored energy and on the efficiency of the propulsion system, from propellers to the energy storage [8]. It is well known that efficiency and power density are conflicting requirements.

As in all aeronautic applications, even if they do not carry people or dangerous payload onboard, standards in terms of safety are particularly stringent [9], [10]. So far, several studies are reported in the literature, aiming to increase the resiliency of these systems through appropriate control in case of failure. For example, Vey and Lunze [11] analyze the condition of a complete rotor loss for both a quadrotor and a hexrotor. In the latter case, thanks to its redundancy, through a reconfiguration of the control system, just a soft failure is experienced with a decrease of maneuverability. However, for a quadrotor UAV, the complete rotor loss can result in moderate or even catastrophic failure, especially when the weight increases. In [12] and [13], different approaches have been investigated to avoid crashes in such conditions. Nevertheless, if the thrust is lost in one rotor, the mission capabilities are surely compromised and the more the weight the more crucial safety aspects are. While redundancy helps to prevent catastrophic failures, it is also clear that it comes at the expense of power density.

Adoption of a multiphase configuration is another approach that can be used to increase the resiliency of electric drives since they are still able to operate after a phase winding or inverter leg fault [14], [15]. While this option is given high consideration for more electric aircraft or fully electric aircraft applications [16], the scenario is completely different in the field of multirotor UAVs, where the most common approach is to use a commercial power converter and machine [17]. This consideration leads to suggesting that the application of multiphase configurations to multirotor UAVs is still an open research field. Also in this case, however, attention should be paid on the effects of this design choice on the overall drive weight and size.

Finally, thermal design is another critical aspect to consider, since not only it allows to extend the flight endurance, but it also strongly impacts lifetime and therefore reliability of components. However, increasing reliability through proper thermal

---

Manuscript received December 6, 2019; revised March 18, 2020, May 24, 2020, and July 13, 2020; accepted July 25, 2020. Date of publication August 4, 2020; date of current version October 30, 2020. This work was supported part by Infineon. Recommended for publication by Associate Editor Prof. Dian Guo Xu. *(Corresponding author: Federico Marcolini.)*

Martin Schiestl, Maurizio Incurvati, Ronald Stärz, Alejandro Secades Rodríguez, and Lukas Wild are with the Department of Mechatronics, MCI Management Center Innsbruck, 6020 Innsbruck, Austria (e-mail: martin.schiestl@mci.edu; maurizio.incurvati@mci.edu; ronald.staerz@mci.edu; alejandro.secades@mci.edu; lukas.wild@mci.edu).

Federico Marcolini, Fabio Giulii Capponi, and Federico Caricchi are with the Department of Astronautical, Electrical and Energy Engineering, University of Rome “La Sapienza,” 00185 Roma, Italy (e-mail: federico.marcolini@uniroma1.it; fabio.giuliicapponi@uniroma1.it; federico.caricchi@uniroma1.it).

Color versions of one or more of the figures in this article are available online at https://ieeexplore.ieee.org.

Digital Object Identifier 10.1109/TPEL.2020.3013899

design is another requirement that conflicts with the power density one.

Following the previous considerations, this article presents a propulsion system that aims to achieve the high power density targets for UAVs, while at the same time demonstrating high efficiency and addressing the resiliency and reliability requirements. The considered application is a heavy quadrotor UAVs that operate inside buildings and therefore the overall size is limited to ensure maneuverability.

Keywords to reach the desired goal are integration and modularity. Integrated motor drives, and particularly integrated modular motor drives (IMMD), have been successfully proposed in traction applications for electric vehicles, which share similar requirements with UAV propulsion [18]–[20], but nothing has been reported until now related to drones.

This article focuses its attention mostly on the power electronic converter, leaving the detailed discussion of the electric machine and the overall control to future publications. It is structured as follows. Section II gives an overview of the entire propulsion system, discussing and justifying the main design choices. Section III presents the modeling of the inverter and its analysis through simulations. Section IV reports the results of the experimental tests. Finally, the conclusion is drawn in Section V.

II. SYSTEM OVERVIEW

The propeller design choice strongly impacts the design of the electrical machine and the related power electronic converter.

Increasing the propeller diameter allows us to obtain higher thrust for a given mechanical power at the shaft [21], but on the other side, it also limits the maximum operating angular speed, due to the constraints on the tip speed. On the contrary, the propeller loading, P_L, equal to the thrust per unit propeller area, can be maximized when reducing the diameter.

Therefore, a tradeoff between dimensions, weight, and thrust needs to be achieved [22]. The analysis presented in Section II-A shows that the optimal sizing is found at a relatively small propeller diameter and high rotational speed. In fact, this solution allows us to maximize the specific propeller loading, P_{Lspec}, defined as the ratio of the propeller loading with respect to the mechanical power. As a consequence, also the powertrain power density can be maximized: in fact, not only the propeller will be smaller and lighter, due to the reduced dimensions, but also the electric machine power density will benefit from the increase in speed.

Following this design choice, it results that the maximum operating fundamental frequency also increases, exceeding the kHz threshold. At these levels, two challenges arise. On the electrical machine side, the design shall take appropriate measures to limit frequency-dependent losses; on the converter side, an increase in switching frequency becomes necessary to ensure good quality of the waveforms and accurate current control, with a consequent impact in terms of losses [23].

The resiliency of the drive is ensured through a multiphase arrangement. In particular, a twelve-phase system is chosen, since this allows arranging the winding of the machine in four independent three-phase systems, each with its own neutral point. The power electronic converter can also be split into four three-phase inverters: in this way, smaller and faster power components can be used, with several benefits in terms of passive components size, EMC, and bandwidth. This solution allows us to implement both traditional control algorithms and fault tolerant control strategies. In fact, in case of failure in one phase, the entire three-phase subsystem can be easily taken out of service. The drive will however continue to operate with the remaining healthy windings at rated power for a finite amount of time or at 75% of rated power indefinitely.

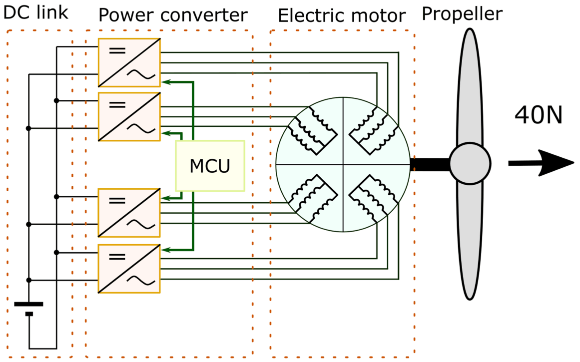

Fig. 1. Schematic depiction of the electric system.

The design of the powertrain features a high degree of integration: in fact, the mechanical frame carries out different tasks at the same time. It works as a mechanical support for the inverters and the electrical machine; it behaves as a mechanical interface between the drive and the drone's framework, and, finally, it is the heat sink through which the heat is removed from within both the machine and converter. This arrangement allows us to significantly increase the power density, to simplify the connections by the elimination of power cables and also to mitigate possible EMC problems, [18], [20], actually increasing the reliability of the drive.

Fig. 1 shows a schematic view of the powertrain, where the propeller is directly coupled to the multiphase electric drive, while the electrical machine, the power electronic converter and the control board are all enclosed in the same housing.

Moreover, the massive airflow generated by the propeller on its axis is used as a forced air cooling mechanism for the frame. Therefore, as shown in Fig. 2, since the motor and the power electronic converter are integrated into the same housing, mechanical and thermal functions can be merged together, to increase the power density.

A. Propeller Selection

The propeller is required to exert a thrust of at least 40 N, to carry the payload and to achieve a feasible flight ability. The study of the suitable propeller geometry is realized in a range of low flight speeds on the vicinity of such the UAV will foreseeably perform (from 1 to 9 m/s, without any inclination angle of the flight velocity vector). In particular, as already discussed, the propeller diameter needs to be optimized to find

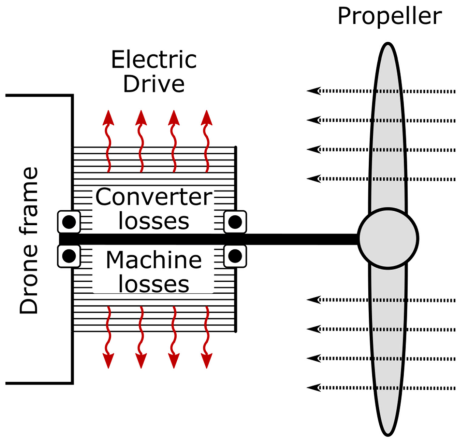

Fig. 2. Schematic view of the mechanical system.

TABLE I
COMPARISON OF DIFFERENT PROPELLERS

	Prop A	Prop B	Prop C	Units
Speed	15000	6500	6500	rpm
# of blades	8	2	8	-
Power	1000	600	1000	W
Diameter	0.34	0.81	0.31	m
Thrust	45.49	45.56	45.98	N
PL	501.14	88.42	609.17	N/m^2
PL spec.	0.501	0.1474	0.6092	N/Wm^2

the best compromise between thrust-to-power ratio and propeller loading, keeping in mind the limitations that constrain its size [24]. For this design, a maximum value for the tip speed of 0.8 Mach number has been considered as a limitation for the propeller diameter.

An iterative software in MATLAB has been developed, based on the combined Momentum & Blade Element theories for minimum loss condition without neglecting wake contraction as developed and described in [25]. The software develops the optimal propeller geometry and determines its performances in parametric form as a function of the number of blades, airfoil data type (or types), hub diameter, and atmospheric conditions.

Table I shows a comparison of three propellers designed according to different optimization objectives. In propeller B, the thrust-to-power ratio is maximized, resulting in the design with the highest diameter, which limits the maximum speed to 6500 r/min. Propeller C, instead, is designed by optimizing for specific propeller load P_{Lspec}, while propeller A represents the concurrent optimization of specific propeller load and total weight, including its structure. All the designs need to comply with a minimum thrust of 45 N.

A comparative analysis shows that propeller A is smaller, lighter and has much greater P_L and P_{Lspec} than propeller B, at a maximum speed of 15 000 r/min. It is interesting to note that propeller C only slightly outperforms design A in terms of specific propeller load P_{Lspec}. However, propeller C results in a much heavier structure with much wider chords and greater thickness of the blades and therefore shows a low thrust-to-weight ratio, jeopardizing the specific power figure. In addition, the lower design speed at the same power reduces also the power density of the electrical machine.

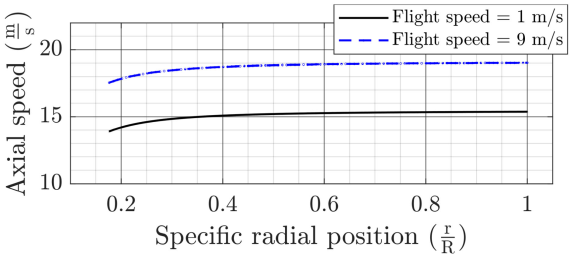

Fig. 3. Axial velocity at propeller vicinity, straight up- and downwind.

From the above-mentioned analysis, it can then be concluded that propeller A is the optimal design in terms of power density: it develops about 45 N of thrust at 15 000 r/min and 1 kW mechanical input power. The noticeable observation from this analysis is that optimizing at the same time for thrust-to-weight ratio and specific propeller load leads to high-speed designs, in excess of 10 000 r/min and in contrast to what is commonly found in the literature. All that has a significant impact on the overall drive design.

Given the highly integrated design, it is important to study the axial air flow, since it runs over the outer surface of the housing and determines cooling capabilities. When the UAV is in flight mode, the resulting air axial speed is shown in Fig. 3 as a function of the propeller radial position and for flight speeds of 1 and 9 m/s. A very flat behavior is obtained, with a minimum of 15 m/s. In hovering mode, instead, air axial speed is proportional to the square root of the thrust [24]: when this last one is equal to 45 N, an axial air flow of 14 m/s is still found. This analysis allows us to calculate the heat transfer coefficient for the thermal design of the drive and confirms that it is going to remain pretty much constant in every operating condition.

B. Electric Motor

Coming to the electrical machine design, an axial flux permanent magnet (AFPM) machine is considered, since it has already been proven that this machine allows greater torque density than its radial counterpart [26]. The chosen topology is the torus-type, having two rotors and one stator in between [27].

Due to space constraints, manufacturing problems cannot be overlooked, thus the number of coils has been fixed to 12, i.e., the minimum number that allows us to obtain four different three-phase subsystems. Concentrated windings [28], [29] are also adopted both for the ease of manufacturing and because a significant reduction in the mutual coupling between phases is obtained, thus increasing the resiliency of the drive in case of fault. Furthermore, when concentrated windings are adopted, the end-windings do not overlap: as a consequence, in case of fault, the local over-temperature of the faulty phase does not affect the healthy ones.

From the fractional slot theory [30], it is found that the best tradeoff in terms of flux linkage and harmonic behavior

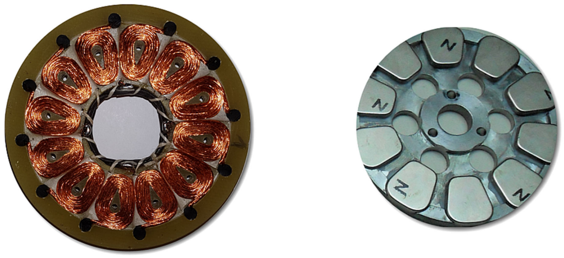
(a) (b)

Fig. 4. Electric motor prototype. (a) Stator twelve-phase concentrated winding. (b) One rotor disk with magnets.

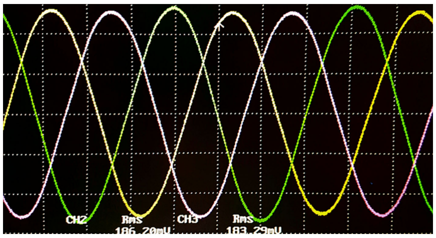

Fig. 5. One three-phase subsystem back emf measurements (100–10 ms/div).

TABLE II
Performances of the Electric Machine

Parameter	Value
Rotor pole	10
Number of coils	12
Mechanical speed	15000 rpm
Rated torque	0.7 Nm
Rated current	15 Arms
Rated frequency	1250 Hz
Efficiency	95%
No-load phase voltage (@1250 Hz)	5.8 Vrms
Phase inductance	4 µH
Phase resistance	12 mΩ

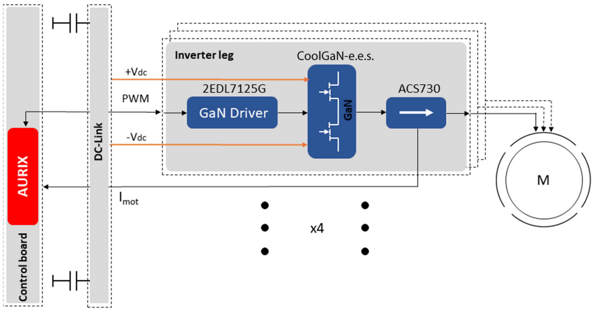

Fig. 6. Overview of the electronic system including control MCU, power electronics, and sensors.

is obtained with a number of rotor poles equal to 10. This sets the fundamental frequency at 1250 Hz, when the speed is 15 000 r/min. At such frequencies, losses mitigation becomes critical because otherwise the powertrain efficiency (and UAV's flight endurance) would be significantly affected. Moreover, as the size reduces with the increase in power density, it becomes more and more difficult to extract the heat within the desired temperature limits. For this reason, a coreless AFPM structure has been chosen, so that iron losses are eliminated, together with a Litz wire winding to limit ac losses in the copper. It is worth noting that the absence of the iron core further decreases the mutual coupling between the phases. Details on the design of a coreless AFPM machine with nonoverlapping concentrated windings can be found, for example, in [31] and [32].

Fig. 4 shows the prototype of the twelve-phase coreless Torus-type AFPM machine with nonoverlapped windings that have been built. Fig. 5, instead plots, a diagram of the machine's no-load voltages taken during preliminary experimental testing. As it is expected, since each coil spans 150 electrical degrees, the resulting waveforms are very close to sinusoidal.

Finally, the main machine parameters are listed in Table II.

C. Inverter Description

Consistently with the machine structure, the power electronic converter is composed of four three-phase inverters. Rated input voltage is 24 V so that the system can be supplied by six series connected Li-Po cells; rated output current is 15 Arms at a rated frequency of 1250 Hz.

At such high fundamental frequencies, wide-bandgap devices have already shown to allow for higher power densities and efficiency than their silicon counterparts, especially in IMMD [19]. In particular, for this design, Infineon CoolGaN early engineering samples (CoolGaN-e.e.s.) are chosen.

Those are discrete components, with a single GaN switch per integrated circuit, rated 100 V and 40 A. One particular feature of this device is related to its packaging: in fact, the silicon substrate is exposed at the GaN topside, without any additional plastic cover, thus allowing a very low-thermal resistance path for losses extraction. At the present time, however, these devices are not available for a voltage rating that matches more precisely the dc-link voltage.

A block diagram of the converter is shown in Fig. 6. It is composed of one control board, equipped with an Infineon Aurix TC233 automotive grade micro-controller, and one main dc-link board plus twelve PCBs each of them realizing an half-bridge module. Every half-bridge module mounts.

1) Infineon GaN bootstrap driver 2EDL7125G.
2) Infineon low voltage CoolGaN-e.e.s.;
3) Allegro Hall-Effect current sensor ACS730, with 1 MHz bandwidth.

Such a modular structure allows full integration between the converter and the electrical machine. In fact, each module is located in direct correspondence with each coil, as schematically shown in Fig. 7, eliminating interconnection cables. As a result, no connectors are needed (one of the major sources of faults), losses and additional voltage drops are eliminated, EMI and possible overvoltage problems are strongly limited. Moreover, in case of fault, it is possible to completely switch OFF one half-bridge module or one entire inverter, taking full advantage of the multiphase arrangement.

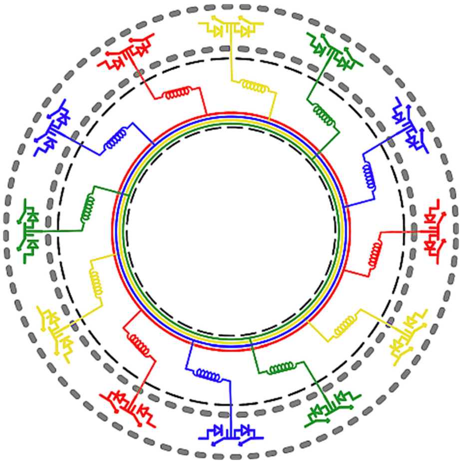

Fig. 7. Distribution of the half-bridges of the four inverter systems.

TABLE III
POWER ELECTRONIC CONVERTER RATED PERFORMANCES

Item	Value	Description
V_{dc}	24 V	DC-link voltage
N_{ph}	12	Number of phases
I_{ph}	15 A	Rated phase current
f_{out}	1250 Hz	Rated fundamental frequency
η	96%	Rated efficiency
f_{sw}	200 kHz	Switching frequency
t_{dead}	100 ns	Dead time
$C_{dc,HB}$	$5 \times 4.7\ \mu F$ $/100\ V$	DC-link capacitors on Half-bridge PCB
$C_{dc-link}$	$24 \times 4.7\ \mu F$ $/100\ V$	DC-link capacitors on main DC-link PCB

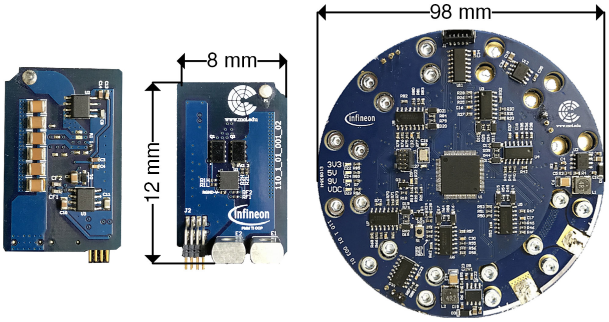

Fig. 8. (a) Bottom and (b) top views of half-bridge board module. (c) Control electronics board mounted on dc-link PCB.

The main characteristics of the converter are summarized in Table III, while Fig. 8 shows the prototypes of one half-bridge module PCB and the control board directly mounted on the dc-link PCB.

The whole UAV is composed of four propellers with their integrated propulsion systems and a main body equipped with redundant central controllers (see Fig. 9). Each local Aurix TC233 micro-controller implements a sensorless vector control scheme for each of the four inverters. The sensorless algorithm is based on a back-emf estimation algorithm and used hall-effect position sensors for safe a reliable start-up. A space vector modulation scheme (SVPWM) is adopted to command the GaN switches.

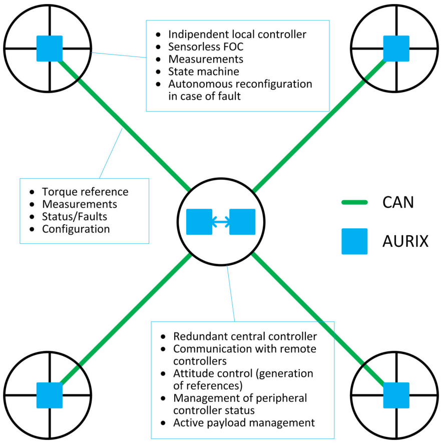

Fig. 9. Overall control structure of the UAV with redundant central controllers and independent local controllers.

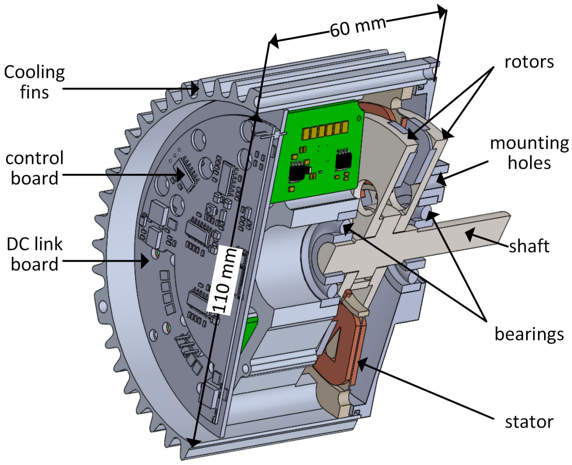

Fig. 10. Three-dimensional cross section of the full assembly.

D. Powertrain Integration

Fig. 10 shows a cross section of the 3-D drawing with all components assembled. Starting from the right, it is possible to notice the shaft, where the propeller is going to be mounted; the AFPM motor, composed of two rotors and one stator in between; the twelve half-bridge PCB modules, mounted radially in correspondence with each coil; the dc link and control boards. Mounting holes are also visible, that are used to anchor the drive to the drone framework, and also the bearings that are placed on the front shield and the housing structure.

Correct radial positioning of the half-bridge PCB modules is ensured through screw terminals on the dc-link board. Each module is then pressed through a metallic clip against one of the twelve aluminum spokes, which act both as a mechanical support and as a thermal extraction path. In fact, the clip directly presses the top side of each GaN against the aluminum (see Fig. 11).

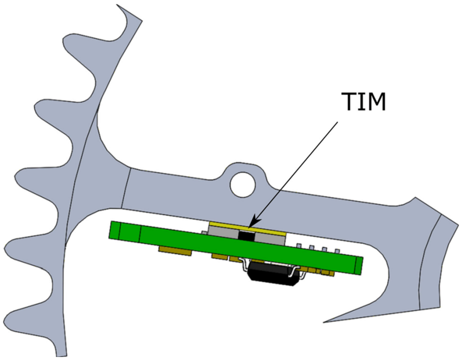

Fig. 11. Detail of half-bridge PCB positioning. The top side of the GaN is pressed to the aluminum frame through a thermal interface pad (TIM).

TABLE IV
POWER DENSITIES OF THE ELECTRIC DRIVE

Item	Weight	Power densities
Electric Motor	410 g	2.43 kW/kg
Power converter	152 g	9.47 kVA/kg
Frame and covers	560 g	
Bearings, shaft …	122 g	
Overall	1.24 kg, 0.698 *l*	0.83 kW/kg, 1.43 kW/*l*

Electrical insulation between the source terminal of the device and the aluminum frame is guaranteed by a thermal interface pad. This solution is intended to minimize the thermal resistance from the top side of the GaN to the ambient. The clip, therefore, allows the mechanical frame to carry out both its mechanical and thermal functions.

Finally, the external frame is designed to provide a totally enclosed manufacturing and is equipped with fins along the axial direction thus taking advantage of the air flow caused by the propeller and therefore decreasing the thermal resistance between ambient and frame. Table IV lists the size and weights of the different components and calculates the expected power densities. The power density of the overall drive, considering the cylindrical bulk volume, is approximately 1.43 kW/*l*, which is a very good result if it is compared to [33], where a value of 0.71 kW/*l* was reached. In addition, the breakdown of the weights shows that frame and covers are still a significant part of the overall system. It is therefore possible to further optimize the geometry of the mechanical frame to reduce weight and size and to increase the overall power density.

E. Considerations on Vibrations

Due to its intrinsic modularity, the proposed concept has the potential to increase the availability and safety of the overall system. It is however worth to point out that vibrations have to be carefully measured in real operating conditions to evaluate their effect on the overall reliability. Nevertheless, the system has been designed to limit the effect of vibrations basing on the following assumptions.

1) The motor is a slot-less, coreless, type. Therefore, cogging torque and consequent vibrations are not present.
2) The connection among the 12 half bridges and the stator is flexible.
3) TIM provides a soft surface between electronics and aluminum housing.
4) The overall structure is stiff with resonant modes located at the higher frequencies.

Furthermore, standard inverters not integrated into the motor would experience on UAV similar level of vibrations and accelerations having the disadvantage of being not modular and therefore providing a lower reliability/availability.

III. INVERTER MODELING

This section describes the modeling of the inverter that has been carried out to confirm the efficiency specification and to predict both its transient and thermal behavior. First of all, a loss analysis calculation is described and afterward an equivalent circuit that takes into account all parasitic phenomena is developed. Finally, a thermal analysis is also performed through the software Ansys Icepack.

A. Losses Estimation

A first estimation of the GaN losses, and the efficiency of the whole power electronic converter, can be obtained using (1), (2), [34], and (3)–(5)

$$P_{c,\text{pos\_half}} = R_{\text{dson}}\, I_{pk}^2 \left(\frac{1}{8} + \frac{m_a}{3\pi}\cos\phi\right) \tag{1}$$

$$P_{c,\text{neg\_half}} = R_{\text{dson}}\, I_{pk}^2 \left(\frac{1}{8} - \frac{m_a}{3\pi}\cos\phi\right) \tag{2}$$

where m_a is the modulation index and cosϕ is the displacement power factor

$$P_{c,\text{tot}} = \frac{R_{\text{dson}} I_{pk}^2}{4} \tag{3}$$

$$P_{sw} = \frac{1}{\pi}\, V_{dc} I_{pk} \left(t_r + t_f\right) f_{sw} + \frac{1}{2} C_{oss} V_{dc}^2 f_{sw} \tag{4}$$

$$P_{\text{dead}} = f_{sw}\ \ \text{t}_{\text{dead}}\ \left[\frac{2\text{V}_{\text{SD}}\text{I}_{\text{pk}}}{\pi} + \text{R}_{\text{dsoff}}\left(\frac{\text{I}_{\text{pk}}^2}{2} + \Delta I^2\right)\right] \tag{5}$$

where P_{c,pos_half} and P_{c,neg_half} are the conduction losses of the switch, respectively, during the positive and the negative half cycles of the sinusoidal current, $P_{c,tot}$ are the average losses of the GaN over a fundamental cycle, P_{sw} are the switching losses including the term related to the output capacitance, and P_{dead} are the losses occurring during the dead-time. In (5), R_{dsoff} is the differential resistance and V_{SD} is the reverse operation voltage of the channel both at $V_{\text{GS}} = 0$ V: taken together they model the reverse drain-source characteristic and allow to calculate the conduction losses during dead-time. All parameters are defined in Table V. The current ripple ΔI can be calculated from the dc-link voltage, V_{dc}, the amplitude modulation ratio, m_a, and the machine inductance. For the selected switching frequency of 200 kHz, it is estimated to be approximately 4 A. Once the current ripple is known, it is also possible to estimate the losses

TABLE V
CHARACTERISTICS OF COOLGAN-E.E.S. SWITCHES

Item	Value	Description
V_{DS}	100 V	Continuous drain-source voltage
I_D	40 A	Continuous drain current
R_{dson}	3 mΩ	GaN channel resistance in on state
R_{dsoff}	15 mΩ	Reverse drain-source conduction differential resistance at V_{GS}=0V
$t_{r(f)}$	20 ns	Rise (fall) time during switching
C_{oss}	350 pF	Output capacitance
V_{sd}	1.75 V	Reverse operation voltage at V_{GS}=0V
ΔI	4 A	Peak-to-peak current ripple
$P_{loss,GaN}$	*2.3 ± 0.3 W*	Calculated losses (single GaN)
$P_{loss,tot}$	*55.2 ± 7.2 W*	Calculated losses (whole converter)

TABLE VI
MOSFET VERSUS GaN COMPARISON

Item	MOSFET OptiMOS BSC028N06NS	GaN CoolGaN-e.e.s.
V_{DS}	60 V	100 V
I_D @ 25°C	100 A	40 A
R_{dson}	2.8 mΩ (@V_{gs}=10V)	2.8 mΩ (@V_{gs}=5V)
R_{gate}	7 Ω	15 Ω
$R_{th,jc}$	*1.4 °C/W (bottom side), 20 °C/W (top side)*	*0.5 °C/W (top side)*
Power losses	2.3 W	2.3W
Dimensions	5 mm x 6 mm	3 mm x 5 mm

for a single GaN according to (3)–(5). The lower part of Table V shows the estimated losses at nominal operating conditions.

The evolution of the losses over an electric period is shown in Fig. 12(a) for the case of a top switch. Instead, Fig. 12(b) plots the losses of one three-phase inverter as a function of the phase current and the modulation index. The same plot shows also the constant output power curves for the electrical machine so that inverter losses can be identified in each operating condition. Finally, Fig. 12(c) shows the relative behavior of losses and current ripple for different choices of the switching frequency. In the analyzed range, converter losses decrease almost linearly with frequency, but the current ripple increases more than linearly in the range between 150 and 200 kHz. Therefore, the value of 200 kHz was selected as an overall compromise to limit the current ripple, resulting in lower harmonic losses inside the machine and better controllability.

It is also interesting to perform a brief comparison between the selected device and a similarly rated MOSFET (i.e., OptiMOS BSC028N06NS). The main results of the comparison are summarized in Table VI; the gate resistance is optimized to obtain ideally the same switching transients under the assumption that the parasitic inductances remain the same (not true in practice since the MOSFET has a much greater internal parasitic value). Under these hypotheses, the two devices show the same losses, but the MOSFET exhibits much higher junction-to-case thermal resistance (because of the plastic covering of the top). Furthermore, the surface area of the GaN is also half with respect to the MOSFET, which leads to double power density at the device level. All those considerations confirm the need to adopt wide-bandgap semiconductors.

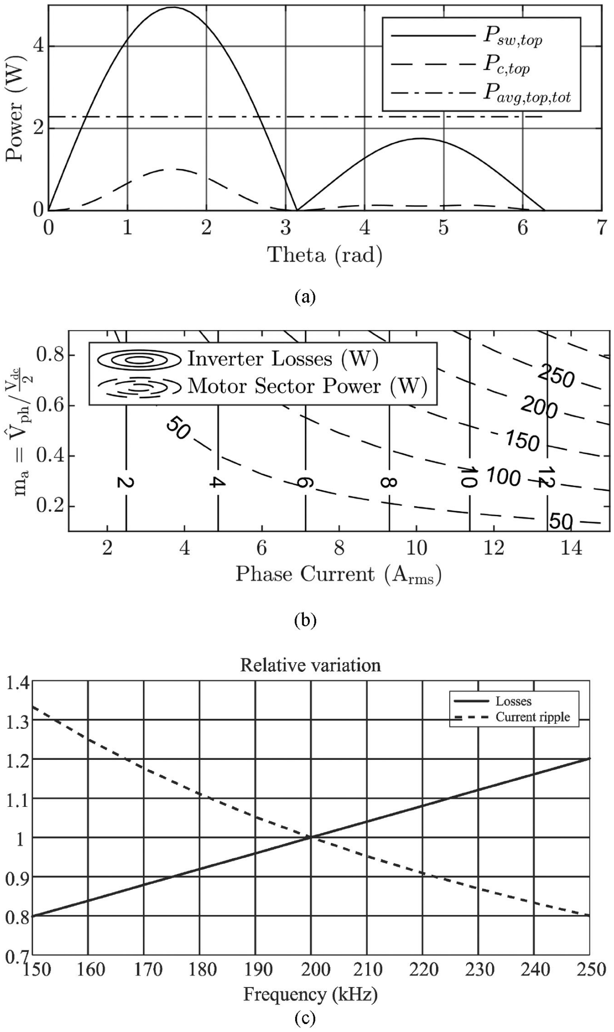

Fig. 12. (a) Instantaneous and fundamental cycle average top switch losses. (b) Total inverter losses of one three-phase inverter and motor output power. (c) Relative losses and current ripple versus switching frequency.

B. Electromagnetic Design and Transient Simulations

The design of the dc-link and half-bridge PCB is critical to ensure system functionality and robustness. Particular care was taken in designing the layout of the latter following well-known best practices to minimize parasitics, such as to position the driver as close as possible to the switch. Rivera-Ramos and Jimenez [35] provide useful equations to obtain an immediate evaluation of parasitic inductances and capacitances, to check if changes in the layout were needed.

Once the layout was finalized, PCB parasitic capacitances were determined through electromagnetic simulation with the software Q3D. The only capacitances of interest are the ones between phase traces and power lines: results led to an estimation of $C_{\mathrm{par,high}} = 3.18$ pF between the phase trace and the positive dc-link bus and of $C_{\mathrm{par,low}} = 2.51$ pF between the phase trace and the negative dc-link bus, (see Fig. 13).

In terms of parasitic inductances, instead, several traces are of interest: the gate lines to the switches as well as the power

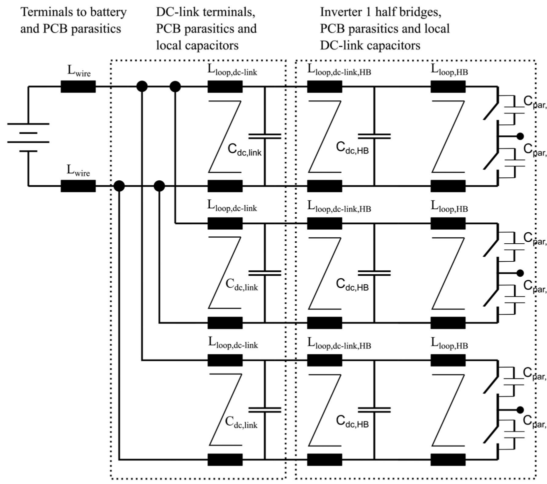

Fig. 13. Arrangement of HB and main dc-link capacitors and parasitics for LTSpice simulation of the capacitors' current.

TABLE VII
PARASITIC INDUCTANCES AND RESISTANCES FOR THE INVERTER BOARD

Path	L_{CALC} (nH)	L_{SIM} (nH)	R_{SIM} (mΩ)
L_{GateHOH}	4.58	4.51	3.11
L_{GateHOL}	5.59	5.34	3.56
L_{GateLOH}	3.41	2.75	2.60
L_{GateLOL}	5.48	4.58	3.99
$L_{\text{loop,HB}}$		3.66	1.30

loop inductance ($L_{\text{loop,HB}}$ in Fig. 13). The gate inductances (L_{GateHOH}, L_{GateHOL} for the high-side switch and L_{GateLOH}, L_{GateLOL} for the low-side switch) have been both calculated analytically according to [36] and evaluated through simulations.

Table VII reports the results of the calculations and the values extracted from the software. The discrepancies at the paths of the low-side gate can be explained by the smaller loop, which reduces the self-inductance and is not accounted for in the calculations. In general, however, calculated and simulated valued show a good agreement, ensuring their correct estimation.

The above-mentioned values of the parasitics were used for transient simulations with LTspice, to more accurately recreate the real switching behavior of the devices. A comparison between simulation and measurements of the transient behavior of the switches has been carried out. An example of the turn-ON transient is shown in Fig. 14. As it can be observed, the simulation, Fig. 14(a), and the measurement, Fig. 14(b), match quite well. The oscillation frequency as well as the overshoot exhibit a good agreement, which confirms the correct evaluation of the parasitics. A small discrepancy of 5 ns can be still observed in the rise time, which can be explained as a nonperfect modeling of the GaN or of the gate drive circuit.

Once the parasitics are determined, the optimal sizing of the dc-link capacitors can be addressed [37]–[39]. The number and value of the capacitors have been selected according to [40] taking especially into account: the nominal current of the drive, the temperature increases and therefore lifetime, the need for low inductance path in the switch layout, mechanical constraints and vibrations, optimized current/volume ratio, possible EMI issues, and battery ripple current.

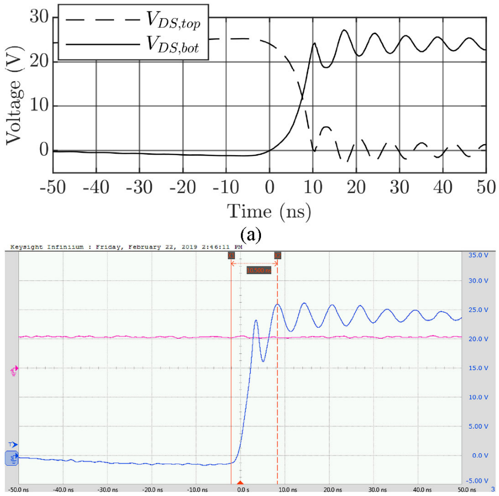

(a)

(b)

Fig. 14. Turn-OFF transient of a bottom switch. (a) LTSpice simulation. (b) Measured waveform (10 ns/div 10 V/div).

The amount of parallel capacitors is mainly depending on their rms current $I_{c,\text{rms}}$ which can be initially estimated through the following equation [41]:

$$I_{C,\text{rms}} = I_{ph}\sqrt{2m_a\left[\frac{\sqrt{3}}{4\pi} + \cos^2\phi\left(\frac{\sqrt{3}}{\pi} - \frac{9}{16}m_a\right)\right]}. \quad (6)$$

A more detailed calculation of the currents present at $C_{\text{dc,HB}}$ can be performed through an LTspice simulation of one half bridge, including $C_{\text{par,high}}$ and $C_{\text{par,low}}$ as well as $L_{\text{loop,HB}}$, as shown in the right end of Fig. 13. These simulation shows, in a worst-case operating scenario, a dc-link capacitor current of the half-bridge PCB equal to $I_{C_{\text{dc,HB,RMS}}} = 6$ A which is in agreement with the initial analytical estimation of (6).

In [19], the capacitor volume as a function of switching frequency is shown for three different capacitor technologies: the comparison clearly demonstrates that ceramic capacitors allow us to minimize the required volume. Therefore MLCC type devices from Murata model GCM32DC72A475ME02 were selected [42].

According to the device datasheet, this would result in a temperature increase of over 35 °C if only one capacitor is used, which reduces to 3 °C when using five parallel capacitors, hence decreasing the individual current to $I_{C,\text{cap,RMS}} = 1.2$ A (see Fig. 15). As an additional benefit, having multiple capacitors in parallel allows us to decrease the power loop parasitic inductance $L_{\text{loop,HB}}$, resulting in smaller overshoot and less stress on the switches as well as in a decrease of the overall losses.

C. Heat Management and Thermal Simulations

The thermal energy generated by the losses of the system needs to be dissipated by the outer structure via forced air-cooling. Fig. 16 shows the thermal circuit of one inverter board

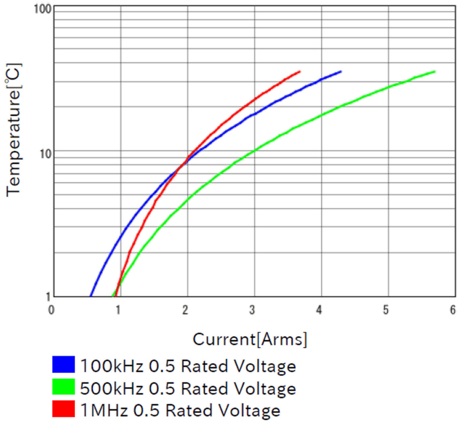

Fig. 15. MLCC capacitors: temperature rise versus current [43].

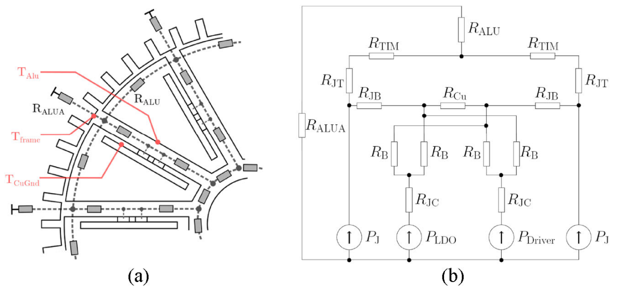

(a) (b)

Fig. 16. (a) Thermal connection on system level. (b) Equivalent thermal circuit from the power sources of one inverter to the medium.

and the thermal connections at the system level as well as the location of the measurement points. The main path followed by the heat flow goes from the switch junction over its top (R_{JT}), through the thermal interface material (R_{TIM})and the aluminum structure (R_{ALU}), till the ambient air (R_{ALUA}). The higher the airflow velocity at the outer frame, the lower the thermal resistance between the frame and the ambient air, R_{ALUA}, will become. Any unbalance in losses between the two switches of the leg will activate also a secondary path from the junction to its bottom (R_{JB}), through the board copper (R_{Cu}) to the bottom of the other switch. The power losses of the driver, P_{Driver}, and the LDO circuitry, P_{LDO}, are two additional power loss sources connected from the junction to their case (R_{JC}).

All inverter sections are thermally connected to each other via the aluminum frame both at the inside and at the outside of the structure.

A finite element thermal simulation of the complete structure is not practicable, since it is very difficult to obtain a converging mesh due to the small airgaps and the round surfaces. Therefore, exploiting axial symmetry, only a 30° section is simulated, stretching it to yield a full orthogonal structure. The half-bridge module PCB with the complete trace layout is exported into Ansys Icepack software, to properly simulate the heat transfer on the board.

Table VIII lists all important simulation parameters, together with the temperatures of relevant spots resulting from the simulation. Additionally, Fig. 17 shows the 3-D temperature map seen from two different angles. Results show that at the nominal power, even at reduced air flow speed conditions (8.1 m/s instead of the nominal value of 15 m/s, to match the experimental test conditions), both the high-side and low-side switch junction temperatures, T_{JHS} and T_{JLS}, are below 60 °C.

TABLE VIII
THERMAL SIMULATION PARAMETERS AND RESULTS

Parameters	Value	Results	Value
P_{GaN}	2.3 W	Airflow velocity	8.1 m/s
R_{JT}	0.5 K/W	T_{amb}	28.49 °C
R_{JB}	1.9 K/W	T_{frame}	37.3-42.0 °C
$\mathrm{R}_{\mathrm{TIM}}$	7.79 K/W	T_{Alu}	40.7-48.9 °C
P_{Driver}	0.2 W	T_{CuGnd}	57.5-59.0 °C
P_{LDO}	0.3 W	T_{JHS}	59.7 °C
		T_{JLS}	59.9 °C

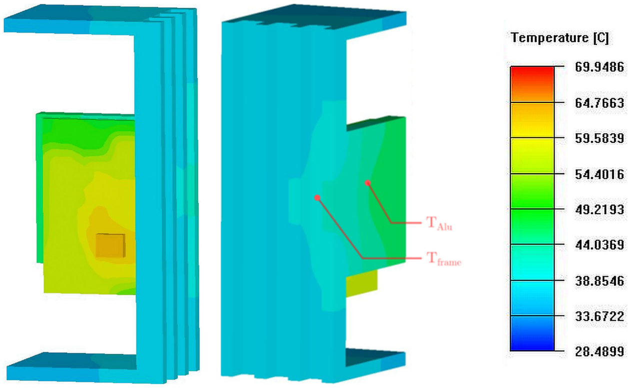

Fig. 17. Thermal maps obtained with ICEPACK.

From the simulations, the equivalent thermal resistance from junction to ambient, R_{Jamb}, can be estimated as

$$R_{\mathrm{Jamb}} = 6.8\,^{\circ}\mathrm{K/W}. \tag{7}$$

The analysis also allows us to evaluate the effectiveness of the constructive solution with no plastic cover on the GaN topside. In fact, from the comparison of the values of R_{TIM} and R_{JT} a ratio greater of 15 is found, clearly showing that the adopted GaN packaging allows for a very efficient heat extraction.

The thermal analysis, however, needs to include also the effects of the losses in the motor, since the aluminum frame is shared with the power electronics converter. The motor power losses are transferred to the aluminum frame through R_{ALU} and then to the ambient through the same frame-to-air thermal resistance of converter, R_{ALUA}. Assuming 50 W of losses in the machine (from the efficiency at rated conditions, Table II) and considering that R_{ALU} is much smaller than R_{ALUA}, it can be estimated that the frame temperature will increase by 13 °C with respect to the value indicated in Table VIII. All other temperatures will also increase by the same amount.

Finally, a transient thermal simulation has also been performed, to evaluate the time constant for the junction and yielding a value of $\tau = 100$ s.

IV. EXPERIMENTAL TESTS

The measurement of the converter power losses and so its efficiency and maximum output power evaluation has several challenges. First, the actual cooling performance of the fins on the housing is directly proportional to the airflow speed produced by the propeller, which is at this stage not available. Additionally, to measure just the losses of the inverter, an external three-phase load is required in place of the motor. Finally, the high number of phases and the high switching frequency and low losses make it very hard to measure the instantaneous output power.

The conventional method, i.e., a direct measurement of input and output power, would require a high precision and very fast instrumentation, which results in high cost, especially for a high number of phases. Therefore, a nonadiabatic semi-calorimetric approach [43], [44] has been adopted, which allows accurate evaluation of total converter losses through multipoint temperature measurements.

The method requires a calibration phase that is usually carried out in dc. It consists in applying a known amount of power losses on the loss carriers and measuring the temperature rise of specific points, equipped with thermocouples. From these measurements, the thermal resistance matrix $\boldsymbol{R}$ can be obtained as

$$\boldsymbol{R} \;=\; {P_{\text{loss}}}^{-1}\,\Delta T \tag{8}$$

where P_{loss} is the power loss vector containing each loss component and ΔT the temperature difference with respect to the ambient temperature.

Once the dc-calibration procedure is completed and the thermal resistance matrix is obtained, (8) is inverted to calculate losses from temperature measurements in the desired operation conditions.

To quantify the error introduced by this method on the evaluation of efficiency and power, both type A and type B uncertainties are accounted for. This results in an overall uncertainty on the temperature δT, which can be calculated through the following equation:

$$\delta T\ (T) = \sqrt{\sigma_{\text{lin}}^2 + \sigma_{\text{rep}}^2\,(T - T_{\text{amb}}) + \sigma_{TC-08}^2\,(T)} \tag{9}$$

whereas σ_{rep} and σ_{lin} are the errors due to reproducibility and linearity, respectively, while $\sigma_{\textit{TC-08}}$ is the error introduced by the thermocouples and the data logger.

The relative error on losses calculation, $\delta P/P$, depends on the relative uncertainty of temperature measurement at the nominal conditions, $\delta T/T$, and depends on the relative error of the thermal resistance matrix, $\delta\boldsymbol{R}/\boldsymbol{R}$. Moreover, since the matrix R needs now to be inverted, there is an error propagation phenomena, which is taken into account with the condition number of the thermal resistance matrix, $\kappa(\boldsymbol{R})$, yielding to

$$\frac{\delta P}{P} \leq \kappa\left(\boldsymbol{R}\right)\left(\frac{\delta T}{T} + \frac{\delta \boldsymbol{R}}{R}\right). \tag{10}$$

A. Measurement Setup

Since at the present stage, the propeller prototype is not available yet, the drive is installed into a wind tunnel (see Fig. 18) to recreate the airflow which would be present if the propeller was mounted on the device. Due to setup limitations, the airflow velocity is set to 8.1 m/s, which is lower than the nominal axial velocity (15 m/s in flight mode).

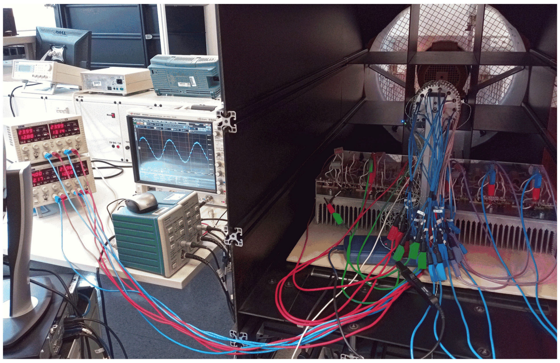

Fig. 18. Measurement setup of the drive. On the left, the power supplies, oscilloscope and current measurement clamps are depicted. On the right, the wind tunnel is visible, together with the UAV drive, the RL loads, and the thermal data logger. The airflow is in the direction into the tunnel.

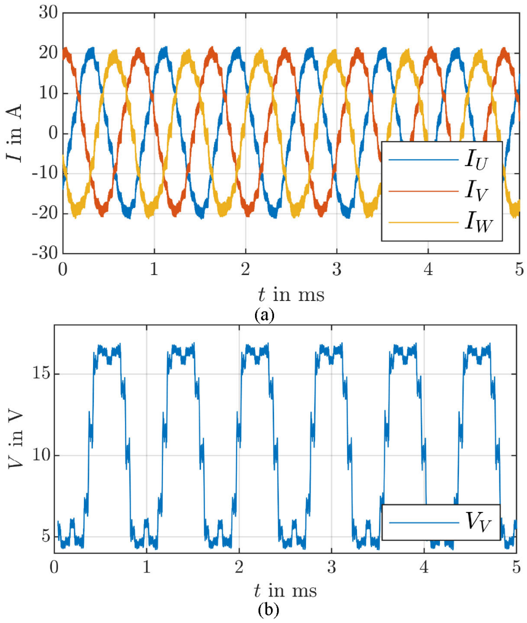

Fig. 19. (a) Phase current and (b) voltage difference between phase and negative terminal of dc-link waveforms on RL load at rated frequency. The voltage waveform is digitally filtered.

While the electric motor is mounted in the integrated drive, it cannot be loaded due to the absence of the propeller. Therefore, tests on the converter have been carried out by using four independent three-phase RL loads with isolated star points. The heatsink mounted resistors and inductors are clearly visible in Fig. 18.

The inductance value was chosen to be 4.2 μH, to match the machine inductance. The selected resistance, instead, was 0.375 Ω. In this way, at the rated current, a voltage drop is produced that is close to the machine's back-emf at rated speed plus the resistive voltage drop on the machine's resistance. As a consequence, the required phase voltage and the modulation index m_a are very similar to the expected ones at rated conditions when the converter is feeding the motor. Fig. 19(a) shows the phase current waveform at 1250 Hz and 15 Arms. For the same conditions, Fig. 19(b) shows the corresponding voltage difference between a phase and the negative terminal of the dc-link; the waveform is digitally lowpass filtered ($f_{\text{pass}} = 40$ kHz,$f_{\text{stop}} = 80$ kHz,

TABLE IX
THERMAL MEASUREMENTS

Parameter	DC-Calibration Value	Nominal Operation
$T_{\text{Alu- Ph10}}$	48.81°C	42.58°C
$T_{\text{DC-Link}}$	49.04°C	49.89°C
$T_{\text{frame-Ph5}}$	46.32°C	40.26°C
$T_{\text{frame-Ph9}}$	45.13°C	39.41°C
$T_{\text{CuGnd-Ph1}}$	71.32°C	65.89°C
$T_{\text{CuGnd-Ph9}}$	71.81°C	63.28°C

$A_{\text{stop}} = -80$ dB) to highlight the fundamental. SVPWM is adopted, consistently to what explained in Section II-B; the control loop is executed every 50 μs (20 kHz).

B. Power Loss Measurement Procedure

Tests have been performed by placing six thermocouples around the system: two on the ground plane of phase 1 and 9 inverter legs, two on the aluminum frame near to phase 5 and 9, one inside the system on the aluminum ribs of phase 9 and the last one on the dc-link. Figs. 16 and 17 show the positions of the above thermocouples.

The dc thermal calibration is performed by imposing a positive current between the negative and the positive dc-link terminals to place all the devices in reverse conduction mode. In this way, it is possible to apply losses homogeneously over all the GaNs (without the need for any gate signal). Moreover, since the reverse conduction equivalent resistance R_{dsoff} is five times higher than R_{dson}, a much lower current is required.

From the temperatures and the applied power, the equivalent thermal resistance and, most notably, the relationship between temperature and power can be calculated. Measurements at different power levels showed an almost completely linear relation between power losses and temperature increase, thus confirming the validity of the nonadiabatic calorimetric approach, even if the calibration takes place at different power levels than the actual operating conditions. Any remaining small deviation is, in any case, still accounted for in (9) by the standard deviation of the linearity error σ_{lin}.

C. Results

For the dc thermal calibration, an amount of power higher than the rated one is fed into the system. This results in higher temperatures, which decrease the relative error made onto the thermal resistance matrix. The reverse input current into the switches is therefore set to 36 A and the reverse voltage of each switch is measured, resulting in a total power loss of 100.05 W for the whole power electronic converter. The resulting calibration temperatures can be seen in the second column of Table IX. By comparing TCuGnd-Ph1, TCuGnd-Ph9, and TAlu-Ph10, it can be observed that the temperature rise of Phase 1 and Phase 9 with respect to the aluminum frame is approximately 25 °C. Since the main focus of this analysis is the calculation of the converter losses and since the temperature of the frame shows an homogenous behavior even at nominal conditions, it is easier to take as a reference the temperature of the frame. Hence, the thermal resistance matrix reduces to the scalar thermal resistance from the switch junction to the frame, R_JALU.

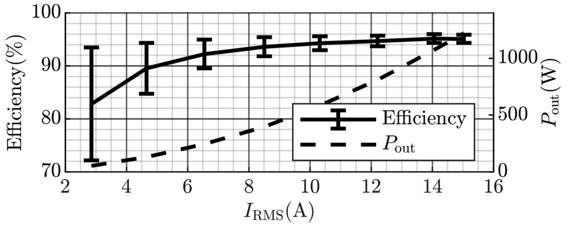

Fig. 20. Efficiency and output power for the total system versus load current rms.

The third colum in Table IX shows the temperature measurements taken during the experimental tests at nominal operating conditions. Comparing the simulated results in Table VIII to the measured temperatures, it can be seen that T_{frame} and T_{Alu} show a good matching, while T_{CuGnd} is off by about 5 °K. However, this result is reasonable, in consideration of the simplifications that were made on the geometry.

Fig. 20 illustrates the efficiency and output power of the whole system as a function of the rms of the phase output current, I_{rms}. The error bars in the efficiency plot are the results of the uncertainties in power calculations, (10), deriving from the uncertainties introduced by the nonadiabatic semicalorimetric approach. At the nominal value of 15 A, the output power P_{out} of the system is 1222 W and the total efficiency is $95.1\% \pm 0.77\%$. The latter results in a total system power loss of 63.1 W ± 9.83 W.

If the total losses of the drivers and LDOs are subtracted (the values for a single module are reported in Table VIII), then the measured value of the total system power losses is in good agreement with the estimated value of the GaN losses that was shown in Table V. Moreover, the nominal power stated in Table III has been reached, leaving headroom for temperature and size as well as power density improvements.

Finally, in terms of transient behavior, the measurements resulted in a system thermal time constant τ equal to 100 s, thus confirming the prediction from the simulations. This result ensures that short overloads will have a low impact on the junction temperature.

Summarizing, despite the complexity of the structure both from a mechanical and an electrical point of view, the adopted analysis and simulation methods have shown to be in very good agreement with measurement results. The developed design strategy is scalable and can be therefore used for a reliable design of bigger systems.

V. CONCLUSION

In this article, a high-power density integrated modular multiphase drive for the propulsion of a UAV was proposed and described. Detailed electrical and thermal analysis for the converter was carried out. Finally, experimental tests were performed to verify the predictions from the model. The key conclusions can be summarized as follows.

1) It is possible to design an electric drive that combines at the same time high power density, high efficiency, and a resilient structure to ensure reliability.

2) To meet the expected requirements, an integrated design approach has to be followed and the frame needs to fulfill both mechanical and heat extraction functions.
3) Adoption of GaN semiconductors at high switching frequency is required to allow at the same time high fundamental frequency and high power density.
4) The predicted overall power density of 1.43 kW/*l* (almost double with respect to the most comparable literature prototype [34]) is confirmed by experimental results.

REFERENCES

[1] A. C. Watts, V. G. Ambrosia, and E. A. Hinkley, "Unmanned aircraft systems in remote sensing and scientific research: Classification and considerations of use," *Remote Sens.*, vol. 4, no. 6, pp. 1671–1692, Jun. 2012.

[2] M. Hassanalian and A. Abdelkefi, "Classifications, applications, and design challenges of drones: A review," *Progress Aerosp. Sci.*, vol. 91, pp. 99–131, May 2017.

[3] R. Mahony, V. Kumar, and P. Corke, "Multirotor aerial vehicles: modeling, estimation, and control of quadrotor," *IEEE Robot. Autom. Mag.*, vol. 19, no. 3, pp. 20–32, Sep. 2012.

[4] R. D'Andrea, "Can drones deliver?," *IEEE Trans. Autom. Sci. Eng.*, vol. 11, no. 3, pp. 647–648, Jul. 2014.

[5] N. Homainejad and C. Rizos, "Application of multiple categories of unmanned aircraft systems (UAS) in different airspaces for bushfire monitoring and response," *Remote Sens. Spatial Inf. Sci.*, vol. XL-1/W4, pp. 55–60, Aug. 2015.

[6] A. Momont, Ambulance Drone tudelft.nl. [Online]. Available: https://www.tudelft.nl/en/ide/research/research-labs/applied-labs/ambulance-drone/, Accessed on: Jul. 22, 2019.

[7] J. Wilke, A drone program taking flight, 2019. [Online]. Available: https://blog.aboutamazon.com/transportation/a-drone-program-taking-flight, Accessed on: Jul. 20, 2019.

[8] O. Gur and A. Rosen, "Optimizing electric propulsion systems for unmanned aerial vehicles," *J. Aircraft*, vol. 46, no. 4, pp. 1340–1353, Jul. 2009.

[9] E. Petritoli, F. Leccese, and L. Ciani, "Reliability and maintenance analysis of unmanned aerial vehicles," *Sensors*, vol. 18, no. 9, Sep. 2018, Art. no. 3171.

[10] M. Waibel, B. Keays, and F. Augugliaro, "Drone shows: Creative potential and best practices," Verity Studios, white paper, 2017. [Online]. Available: http://www.taittowers.com/wp-content/uploads/2017/03/Drone-shows-Creative-potential-and-best-practices.pdf

[11] D. Vey and J. Lunze, "Structural reconfigurability analysis of multirotor UAVs after actuator failures," in *Proc. IEEE 54th Annu. Conf. Decis. Control*, Dec. 2015, pp. 5097–5104.

[12] V. Lippiello, F. Ruggiero, and D. Serra, "Emergency landing for a quadrotor in case of a propeller failure: A PID based approach," in *Proc. IEEE Int. Symp. Saf., Secur., Rescue Robot.*, Oct. 2014, pp. 1–7.

[13] A. Merheb, H. Noura, and F. Bateman, "Emergency control of AR drone quadrotor UAV suffering a total loss of one rotor," *IEEE/ASME Trans. Mechatronics*, vol. 22, no. 2, pp. 961–971, Apr. 2017.

[14] E. Levi, "Multiphase electric machines for variable-speed applications," *IEEE Trans. Ind. Electron.*, vol. 55, no. 5, pp. 1893–1909, May 2008.

[15] L. De Lillo *et al.*, "Multiphase power converter drive for fault-tolerant machine development in aerospace applications," *IEEE Trans. Ind. Electron.*, vol. 57, no. 2, pp. 575–583, Feb. 2010.

[16] 16W. Cao *et al.*, "Overview of electric motor technologies used for more electric aircraft (MEA)," *IEEE Trans. Ind. Electron.*, vol. 59, no. 9, pp. 3523–3531, Sep. 2012.

[17] Q. Quan *et al.*, "An analytical design-optimization method for electric propulsion systems of multicopter UAVs with desired hovering endurance," *IEEE/ASME Trans. Mechatronics*, vol. 24, no. 1, pp. 228–239, Feb. 2019.

[18] N. R. Brown, T. M. Jahns, and R. D. Lorenz, "Power converter design for an integrated modular motor drive," in *Proc. IEEE Ind. Appl. Annu. Meeting*, 2007, pp. 1322–1328.

[19] T. M. Jahns and H. Dai, "The past, present, and future of power electronics integration technology in motor drives," *CPSS Trans. Power Electron. Appl.*, vol. 2, no. 3, pp. 197–216, Sep. 2017.

[20] R. Abebe *et al.*, "Integrated motor drives: State of the art and future trends," *IET Elect. Power Appl.*, vol. 10, no. 8, pp. 757–771, Sep. 2016.

[21] R. W. Prouty, *Helicopter Performance, Stability, and Control*. Melbourne, FL, USA: Krieger, 2002.

[22] P. Pounds and R. Mahony, "Design principles of large quadrotors for practical applications," in *Proc. IEEE Int. Conf. Robot. Autom.*, May 2009, pp. 3265–3270.

[23] S. Li, Y. Li, W. Choi, and B. Sarlioglu, "High-speed electric machines: Challenges and design considerations," *IEEE Trans. Transp. Electrific.*, vol. 2, no. 1, pp. 2–13, Jan. 2016.

[24] J. Roskam and C.T. Lan, *Airplane Aerodynamic and Performance*. Lawrence, KS, USA: DARcorporation, 1997.

[25] C. N. Adkins and R. H. Liebeck, "Design of optimum propeller," *J. Propulsion Power*, vol. 10 no. 5, pp 676–682, Sep. 1994.

[26] A. Cavagnino, M. Lazzari, F. Profumo, and A. Tenconi, "A comparison between the axial flux and the radial flux structures for PM synchronous motors," *IEEE Trans. Ind. Appl.*, vol. 38, no. 6, pp. 1517–1524, Nov./Dec. 2002.

[27] F. Giulii Capponi, G. De Donato, and F. Caricchi, "Recent advances in axial-flux permanent-magnet machine technology," *IEEE Trans. Ind. Appl.*, vol. 48, no. 6, pp. 2190–2205, Nov./Dec. 2012.

[28] L. Alberti and N. Bianchi, "Theory and design of fractional-slot multilayer windings," *IEEE Trans. Ind. Appl.*, vol. 49, no. 2, pp. 841–849, Mar./Apr. 2013.

[29] E. Fornasiero, L. Alberti, N. Bianchi, and S. Bolognani, "Considerations on selecting fractional-slot nonoverlapped coil windings," *IEEE Trans. Ind. Appl.*, vol. 49, no. 3, pp. 1316–1324, May/Jun. 2013.

[30] N. Bianchi, M. Dai Prè, and L. Aliberti, *Theory and Design of Fractional-Slot PM Machines*. Padova, Italy: CLEUP, 2007.

[31] M. J. Kamper, R. Wang, and F. G. Rossouw, "Analysis and performance of axial flux permanent-magnet machine with air-cored nonoverlapping concentrated stator windings," *IEEE Trans. Ind. Appl.*, vol. 44, no. 5, pp. 1495–1504, Sep./Oct. 2008.

[32] B. Xia, J. Shen, P. C. Luk, and W. Fei, "Comparative study of air-cored axial-flux permanent-magnet machines with different stator winding configurations," *IEEE Trans. Ind. Electron.*, vol. 62, no. 2, pp. 846–856, Feb. 2015.

[33] M. Uğur and O. Keysan, "Multi-physics design optimisation of a GaN-based integrated modular motor drive system," *J. Eng.*, vol. 2019, no. 17, pp. 3900–3905, Jun. 2019.

[34] J. W. Kolar, H. Ertl, and F. C. Zach, "Influence of the modulation method on the conduction and switching losses of a PWM converter system," in *Proc. Conf. Rec. IEEE Ind. App. Soc. Annu. Meeting*, Oct. 1990, pp. 502–511.

[35] A. R. Rivera-Ramos and M. Jimenez, "Analytical models for estimating parasitic components in power electronics PCBs," in *Proc. 48th Midwest Symp. Circuits Syst.*, Aug. 2005, vol. 2, pp. 1235–1238.

[36] H. A. Wheeler, "Transmission-line properties of a strip on a dielectric sheet on a plane," *IEEE Trans. Microw. Theory Techn.*, vol. 25, no. 8, pp. 631–647, Aug. 1977.

[37] M. Ugur and O. Keysan, "Design of a GaN based integrated modular motor drive," in *Proc. 13th Int. Conf. Elect. Mach.*, Sep. 2018, pp. 1471–1477.

[38] J. Wang, Y. Li, and Y. Han, "Integrated modular motor drive design with GaN power FETs," *IEEE Trans. Ind Appl.*, vol. 51, no. 4, pp. 3198–3207, Jul./Aug. 2015.

[39] J. Van Damme, L. Verkroost, H. Vansompel, F. De Belie, and P. Sergeant, "A holistic DC link architecture design method for multiphase integrated modular motor drives," in *Proc. IEEE Int. Elect. Mach. Drives Conf.*, May 2019, pp. 1593–1598.

[40] M. Ugur and O. Keysan, "DC link capacitor optimization for integrated modular motor drives," in *Proc. IEEE 26th Int. Symp. Ind. Electron.*, 2017, vol. I, pp. 263–270.

[41] J. W. Kolar and S. D. Round, "Analytical calculation of the RMS current stress on the DC-link capacitor of voltage-PWM converter systems," *IEEE Proc., Elect. Power Appl.*, vol. 153, no. 4, pp. 535–543, Jul. 2006.

[42] Murata Manufacturing Co. Ltd, GCM32DC72A475ME02_ (1210, X7S:EIA, 4.7uF, DC100V) Reference Sheet. [Online]. Available: https://search.murata.co.jp/Ceramy/image/img/A01X/G101/ENG/GCM32DC72A475ME02-01.pdf. Accessed on: May 7, 2020.

[43] H. Li, X. Li, Z. Zhang, J. Wang, L. Liu, and S. Bala, "A simple calorimetric technique for high-efficiency GaN inverter transistor loss measurement," in *Proc. IEEE 5th Workshop Wide Bandgap Power Dev. Appl.*, Oct 2017, pp. 251–256.

[44] M. Schiestl, A. Lösch, M. Incurvati, and R. Stärz, "Accurate losses multi-point non adiabatic calorimetric measurement technique for WBG power converters", in *Proc. PCIM Eur. Digit. Days*, Jul. 2020, pp. 1330–1337.

Martin Schiestl received the bachelor's degree in mechatronics electrical engineering and the master's degree in mechatronics smart technologies from the MCI, Innsbruck, Austria, in 2015 and 2017, respectively.

In April 2016, he began working with the Emerging Applications Laboratory, focusing on the topic of resonant wireless charging, amplifier design, and drive systems.

Federico Marcolini (Student Member, IEEE) received the B.S. and M.S. degrees in electrical engineering, in 2015 and 2018, respectively, from Sapienza-University of Rome, Rome, Italy, where he is currently working toward the Ph.D. degree in electrical engineering.

His main research interests include analysis and design of permanent magnet machines and wide-bandgap-semiconductor-based power converters.

Mr. Marcolini is a Student Member of IEEE Industry Applications Society, IEEE Power Electronics Society, and IEEE Industrial Electronics Society.

Maurizio Incurvati (Member, IEEE) received the M.Sc. degree in electrical engineering with focus on power electronics and the Ph.D. degree from University of Rome "La Sapienza," Rome, Italy, in 1999 and 2005, respectively.

He worked with the National Laboratories for nuclear physics. The subject of the Ph.D. thesis was power converters for particle accelerators. For eleven years, he focused on the development of power converters and control electronics for high-end applications both for science and industry. He later moved to renewable industry in the field of wind turbines where he contributed to the development of a highly modular system of three-phase back to back inverters. Since 2017, he has been with the Department of Mechatronics, MCI Management Center Innsbruck,where he serves as a Lecturer in power electronics and sensors. His present research interests include the field of high-speed drives, power electronics applied to robotics, and GaN/SiC applications.

Fabio Giulii Capponi (Member, IEEE) received the M.S. and Ph.D. degrees in electrical engineering from the University of Rome "La Sapienza," Rome, Italy, in 1994 and 1998, respectively.

Since 1996, he has been with Sapienza-University of Rome, Rome, Italy, where he is a Full Professor of power converters, electrical machines and drives at the Department of Astronautical, Electrical and Energy Engineering. From 2003 to 2004, he was a Visiting Scholar with the Wisconsin Electrical Machines and Power Electronics Consortium (WEMPEC), University of Wisconsin, Madison, WI, USA. He has authored or coauthored more than 90 published technical papers. His current research interests include permanent magnet motor drives and multiphysics design of electrical machines.

Dr. Giulii Capponi was the recipient of the 2014 First Prize Paper Award and the 2016 Third Prize Paper Award, both from the IAS Industrial Drives Committee. He is a Registered Professional Engineer in Italy and is member of the IEEE Industry Applications, the IEEE Industrial Electronics, and the IEEE Power Electronics Societies. He is a member of the IEEE IAS Industrial Drives Committee, the Electric Machines Committee, and the Transportation Systems Committee.

Ronald Stärz received the master's degree in experimental physics from the University of Innsbruck, Innsbruck, Austria.

He has been the Head of the Hydraulic Engineering Laboratory, the University of Innsbruck, until 2008. Since then, he is working at MCI, where he built up the study programs in Mechatronics and the Emerging Applications Laboratory, which he leads since 2016. His work focuses on high-frequency power electronics and on probes for fusion experiments.

Federico Caricchi (Member, IEEE) received the M.S. and Ph.D. degrees in electrical engineering from the University of Rome "La Sapienza," Rome, Italy, in 1988 and 1994, respectively.

From 1991 to 2010, he was with the Department of Electrical Engineering, University of Rome "La Sapienza," serving as a Head of the Department from 2007 to 2010. Since 2010, he has been with the Department of Astronautical, Electrical and Energy Engineering as a Full Professor. He has authored or coauthored more than 100 technical published papers and more than ten national and international patents. His research interests include analysis and design of unconventional electric machines, power electronic equipment, and permanent-magnet motor drives.

Dr. Caricchi is a Registered Professional Engineer in Italy and is a member of the Italian Association of Electrical and Electronic Engineers, the Italian Association for Naval Techniques, and the IEEE Industry Applications Society. He is a member of the IEEE IAS Industrial Drives Committee and Electric Machines Committee. He was the recipient of the 2005 First Prize Paper Award from the IAS Electric Machines Committee.

Alejandro Secades Rodríguez was born in Llangréu, Asturies, Spain, in 1990. He received the graduate degree in aerospace engineering, from the University Alfonso X el Sabio, Madrid, Spain, in 2014, and the master's degree in mechatronics & smart technologies from the Management Center Innsbruck, Innsbruck, Austria, in 2017.

Since 2016, he is currently a Project Developer at the MCI Mechatronics Department. He specializes in a distinct variety of topics with special focus on CFD, aerodynamics, advanced CAD design, and control engineering.

In 2018, Mr. Secades Rodríguez was the recipient of the First Place for the Best Master Thesis in the Austrian Conference of Mechatronics for his thesis "Simulation of Active Vibration Damping of a Wind Turbine," taken place in Graz, Austria.

Lukas Wild received the bachelor's degree in mechatronics/electrical engineering in 2019 from the MCI, Innsbruck, Austria, where he is currently working toward the master's degree in mechatronics/electrical engineering.

Since October 2018, he has been a Project Collaborator with the Emerging Applications Laboratory, working in the field of power electronics and motor control.